communications materials

A Nature Portfolio journal

Article

https://doi.org/10.1038/s43246-025-00821-3

# Ab initio parametrization of a generalized Hubbard model in a molecule displaying chirality-induced spin selectivity



D. K. Andrea Phan Huu [1,2,7], Arianna Cantarella [2,3,7], Pietro Bonfà[2,5,6], Lorenzo Savi[1], Alessandro Chiesa [2,3,4], Anna Painelli [1] & Stefano Carretta [2,3,4] ✉

Chirality-induced spin selectivity (CISS) refers to the interplay between molecule handedness and the electron spin. Despite ample experimental evidence, the mechanism leading to CISS is not fully understood yet. In this work, we present an ab initio study of a chiral molecule that exhibits CISS upon photoinduced electron transfer. Using DFT and TD-DFT we obtain good agreement with experimental absorption spectra, revealing weak electronic coupling between donor, chiral bridge, and acceptor. To accurately capture electronic correlations, we develop a novel approach to derive a multi-orbital Hubbard model describing the chiral bridge, where all parameters are obtained from ab initio CASCI calculations. This offers a versatile framework that can be extended to other molecular systems. Beyond electronic effects, we explore the role of low-energy vibrations, assessing their impact on the inter-site Hubbard parameters and simulating the system's time evolution via unitary dynamics. Our results indicate that electron-vibration coupling leads to a non-negligible spin polarization, highlighting its potential relevance in the CISS mechanism.

Chirality-Induced Spin Selectivity (CISS), first reported in 1999[1], is the preferential transmission of electrons with a specific spin orientation through a chiral medium, and has since attracted significant attention across diverse research fields. Arguably, it has an impressive potential for innovative applications in spintronics[2] and quantum information[3], offering new perspectives for technological advancements. But CISS may also be the key to understand spin-selective processes in biology[4], it can offer strategies for the real-time monitoring of chemical reactions[5], and for enantioseparation[6]. CISS was first observed in photoemitted electrons through a DNA-coated gold substrate[1]. Since then, it has been detected across a broad range of chiral materials, including single molecules, biomolecules and polymers, suggesting that, to some extent, CISS occurs largely independent of the specific system involved, as long as it is chiral. A major step towards technological application of CISS was achieved when the spin-selective transport was observed for bound electrons passing through a chiral medium, positioned between metallic or semiconducting leads. Further electron transport experiments elucidated how CISS is affected by the thickness of the chiral medium or length of the chiral molecule, its relationship with optical activity, the role of the leads, etc…[6] In all these fundamental studies the experimental setup relies on complex interfaces obtained by coupling the chiral system to (often magnetic) leads, or metallic substrates, leaving open the question if CISS is actually made possible by the presence of heavy-atoms, with their characteristic large spin-orbit coupling (SOC). Only recently, CISS was observed in photoinduced electron transfer (PET) in isolated organic chiral molecules by transient electron paramagnetic resonance, proving that CISS emerges also without a metallic substrate[7,8].

A major challenge in the field amounts to bridge the gap between experimental observations and theoretical models. The ideal theoretical model for CISS should yield high spin polarization with a realistic set of parameters, but should also be general enough to describe a wide variety of diverse systems, including amminoacid chains, DNA, polymers and organic $\pi$-conjugated molecules. SOC is an obvious requirement for CISS[9–11]. However, SOC alone cannot explain experimental evidences, particularly in organic systems where SOC is very weak, and cannot justify, by itself, the large spin polarization observed in experiments. Accordingly, microscopic mechanisms for SOC amplification must be proposed and tested. It has already been pointed out that electron correlations, in addition to SOC, can significantly contribute to the emergence of CISS in transport by amplifying

[1]Dipartimento di Scienze Chimiche, della Vita e della Sostenibilità Ambientale, Università di Parma, Parma, Italy. [2]Dipartimento di Scienze Matematiche, Fisiche e Informatiche, Università di Parma, Parma, Italy. [3]INFN-Sezione di Milano-Bicocca, Gruppo Collegato di Parma, Parma, Italy. [4]UdR Parma, INSTM, Parma, Italy. [5]Present address: Department of Physics, Informatics and Mathematics, University of Modena and Reggio Emilia, via Campi 213/A, 41125 Modena, Italy. [6]Present address: Istituto Nanoscienze, CNR-NANO S3, via Campi, 213/A, 41125 Modena, Italy. [7]These authors contributed equally: D. K. Andrea Phan Huu, Arianna Cantarella. ✉e-mail: stefano.carretta@unipr.it

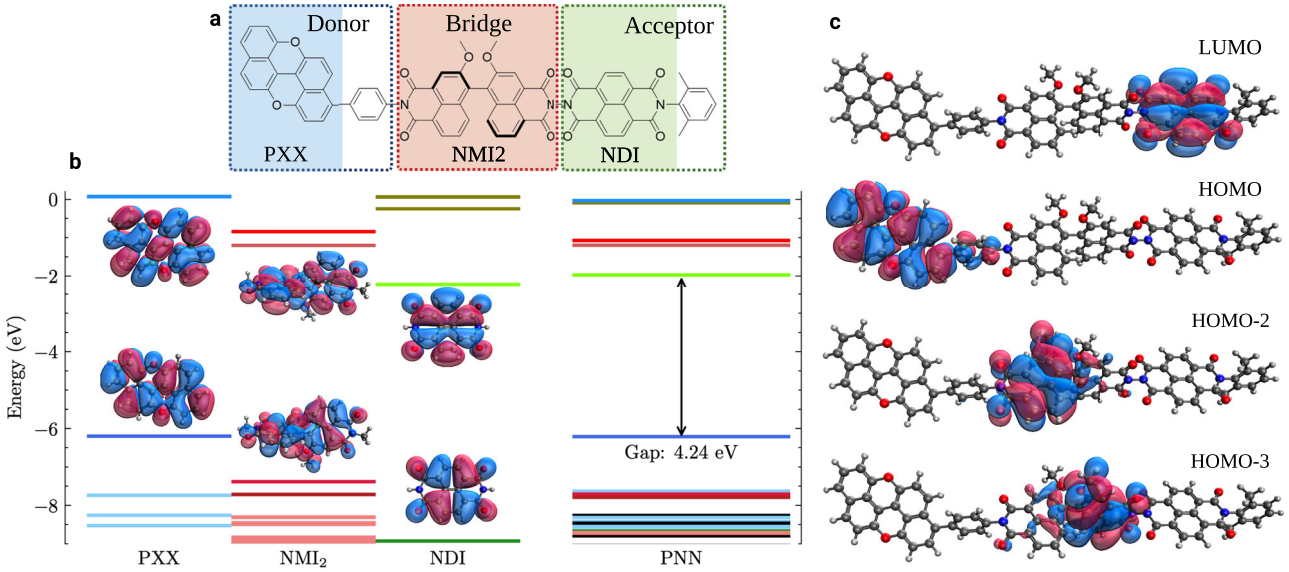


**Fig. 1 | Frontier MOs of PXX, $NMI_2$, NDI, and PNN. a** Kekulè structure of PNN and its partition into donor (PPX), chiral bridge ($NMI_2$), and acceptor (NDI) fragments. **b** The energy levels of frontier MOs, calculated using DFT at the LC-$\omega$PBE/6-31G(d) level of theory ($\omega = 0.196$ $a_0$). On the left, the energy and the iso-surfaces of selected orbitals are shown, as calculated for PXX, $NMI_2$, and NDI fragments. On the right the MOs energies of PNN are shown. The energy levels corresponding to the MOs are color-coded to show how the orbitals from the isolated fragments map onto the orbitals of PNN. The HOMO-LUMO gap of PNN 4.24 eV is also shown. **c** The frontier MOs of PNN. The isovalue of all the isosurfaces is 0.02 $Å^{-3}$.

the spin polarization through electron-electron interactions[12]. Moreover, several studies have demonstrated that temperature and electron-vibration interactions play a significant role in amplifying CISS, suggesting the importance of nuclear degrees of freedom and electron-vibration coupling[13,14]. In a recent work[15] some of us applied a many-body approach to investigate microscopic mechanisms for CISS in PET processes and showed that strong electron-electron correlations can indeed induce a sizable spin polarization. This regime corresponds to a generalized Hubbard model characterized by hopping integrals much smaller than Coulomb repulsion, as typically occurs in molecules such as DNA. In other classes of systems, like conjugated molecules, a different hierarchy of interactions may emerge, often requiring additional mechanisms to achieve large spin polarization values as experimentally observed. Additionally, the development of ab initio methods, properly incorporating many-body effects, is essential for advancing understanding in this field[6].

In this context, we address electron correlations in the charge transfer molecule designed by Wasielewski and coworkers, where CISS was first detected in a PET experiment (Fig. 1a)[7]. The molecule, dubbed here PNN, is formed by the electron donor peri-xanthenoxanthene (PXX), a chiral bridge, i.e., an axially chiral dimer of naphthalene-1,8-dicarboximides ($NMI_2$), and the electron acceptor naphthalene-1,8:4,5-bis(dicarboximide) (NDI) (Fig. S1).

The paper is organized as follows: in Section "Molecular Electronic Structure", we validate against spectroscopic data a *first principle* approch that will then be exploited to address the electronic structure of PNN. The main finding here is that PNN is composed of weakly coupled subunits. This result sets the basis for a discretized model where molecular fragments have well defined localized orbitals to be mapped into an effective Hubbard model. Specifically, in Section "Model Hamiltonian", we adopt a generalized Hubbard Hamiltonian to describe $NMI_2$, the chiral bridge of PNN, and propose an original strategy to extract relevant parameters from ab initio calculations. In Section "The role of SOC and correlation" we critically address the role of electron correlations in PNN, showing that, according to the so-obtained generalized Hubbard model, they actually play a marginal role. In Section "The role of molecular vibrations: assessing low frequency modes", we address the nuclear degrees of freedom of PNN, focusing our attention on the conformational degrees of freedom. This allows us to estimate their impact on specific parameters defined in the Hamiltonian used to model the chiral bridge. The novel strategy proposed here to parametrize the generalized Hubbard model for the chiral NMI bridge is general and can be safely applied to parametrize effective Hubbard models for unbound or weakly bound dimers and larger aggregates. Examples include null aggregates showing symmetry-breaking charge separation[16], or systems exhibiting singlet fission and triplet-triplet annihilation[17], where the interplay between excitonic, localized, and charge resonance states of different spin multiplicity is crucial to the photophysics of interest.

## Results and discussion

### Molecular electronic structure

The system under investigation, PNN, exists as two enantiomers, (R)-PNN and (S)-PNN. In this work, all calculations refer to (R)-PNN (from now on simply PNN), but the discussion applies to both enantiomers. The Kekulè structure of PNN is shown in Fig. 1a, the structures of the PXX, $NMI_2$ and NDI fragments are shown in Fig. S1, and highlighted in different colors in Fig. 1a.

The molecular geometries of PNN and its molecular fragments were optimized using density functional theory (DFT), as described in Section "Methods". Figure 1b shows the energies of the frontier molecular orbitals (MO) and the isosurfaces of selected MOs relevant to PXX, $NMI_2$, and NDI and the entire PNN molecule. In Fig. 1c the relevant MOs for PNN are depicted. These calculations were performed using the LC-$\omega$PBE functional, as described later in this section for the time-dependent DFT (TD-DFT) calculations, with the $\omega$ parameter set to 0.196 $a_0$. A similar version of the b and c plots, generated using the B3LYP functional, is shown in Fig. S3. This comparison highlights the qualitative consistency of the conclusions reported in this paragraph for both functionals. Data in Fig. 1b–c reveal a clear behavior: the MOs are well localized on the different fragments of PNN and the energy levels can be safely ascribed to the separate components. This observation supports treating each fragment separately, as discussed in Sections "Model Hamiltonian" and "The role of molecular vibrations: assessing low frequency modes". Consistent with the donor-bridge-acceptor architecture of PNN, the highest occupied molecular orbital (HOMO) is predominantly localized on the donor unit while the lowest unccupied molecular orbital (LUMO) resides on the acceptor. The chiral $NMI_2$ bridge can be further fragmented into two identical NMI units, so that HOMO and HOMO-1 (LUMO and LUMO+1) of $NMI_2$ are approximately symmetric

and antisymmetric combinations of the HOMOs (LUMOs) of interacting NMI fragments, as illustrated in detail in Section "Frontier orbitals of NMI and NMI2" of the Supporting Information.

Optical absorption spectra of PNN, PXX, NDI and $NMI_2$ collected in toluene at 295 K are reported in ref. 7 and offer the opportunity to validate the picture emerging from first principle calculations. To such an aim, we performed gas phase TD-DFT calculations (Tamm-Dancoff approximation) on PXX, $NMI_2$, and NDI fragments, as well as on PNN. To predict a wide range of states, including localized and charge-transfer states, we employ the optimally-tuned range-separated hybrid functional LC-$\omega$PBE. In this functional the amount of the exact exchange varies with the inter-electronic distance, as defined by a range separation parameter, $\omega$, which is optimized for each system at hand as described in ref. 18, to best simulate ionization potential and electron affinity. A detailed comparison of our simulations with experimental data is provided in Section "TD-DFT calculations" of the Supporting Information, highlighting the excellent agreement achieved, with errors in the predicted transition energies ranging from 0.03 eV to 0.26 eV for the molecular fragments. More to the point, the PNN experimental spectrum can be safely rationalized as the superposition of the absorption spectra of the PXX, $NMI_2$, and NDI fragments. This result, fully confirmed by TD-DFT calculations, strongly supports the fragmentation of the PNN molecule discussed above, relying on the MO analysis.

## Model Hamiltonian

Recent developments suggest that electron correlations beyond mean-field play a major role in CISS[12,13,15,19,20], thus limiting the applicability of mean-field approaches, including the Hartree-Fock and DFT methods. The Hubbard model[21–23] and the analogous Pariser-Parr-Pople model in the chemistry community[24,25] have been successfully adopted to account for strong electron correlations in many different systems, including molecular crystals[26,27], conjugated polymers[28], $\pi$-conjugated dyes[29,30], stable radicals[31,32], and molecular nanomagnets[33–35]. Recently, Chiesa et al.[15] proposed a Hubbard model for electron transfer through a chiral bridge, that yields sizable spin polarization in a photoexcited charge transfer system. The model accounts for nearest neighbor hopping, next-nearest neighbor SOC and strong on site electron-electron correlation with very large $U/t$ ratio for best results. A reliable parametrization of the Hubbard model is therefore needed to validate CISS models. In this section, we propose an original strategy for the ab initio parametrization of a generalized Hubbard model for molecular systems that can be decomposed into (nearly) disjoint fragments, allowing for the assignment of individual *site* orbitals to each fragment. We illustrate this strategy using the chiral bridge, $NMI_2$ (Fig. S1 and Fig. 1a), given its significance in CISS, as discussed in ref. 15. For our purpose, the $NMI_2$ is divided into two equivalent fragments, each representing a distinct NMI unit and corresponding to a site in the Hubbard model (Fig. 2). On each unit, only two MOs are accounted for, a good approximation for the system at hand. The proposed approach is however more general and can be extended to address larger active spaces (Eq. S1). Hence, we propose a generalized Hubbard model describing $NMI_2$ in terms of two identical sites, each bearing two site orbitals as schematically shown in Fig. 2. The relevant Hamiltonian reads:

$$\begin{aligned}\mathcal{H} = &\sum_{I,i,\sigma} \varepsilon_i \hat{n}_{Ii\sigma} - \sum_{I,i,j,\sigma} t_{ij} \hat{c}^{\dagger}_{Ii\sigma} \hat{c}_{Ij\sigma} + \\ &+ \frac{1}{2} \sum_{I,i,j,\sigma} U_{ij} \hat{n}_{Ii\sigma} \hat{n}_{Ij\bar{\sigma}} + \frac{1}{2} \sum_{I,i\neq j,\sigma} \left(U_{ij} - J_{ij}\right) \hat{n}_{Ii\sigma} \hat{n}_{Ij\sigma} + \\ &+ \frac{1}{2} \sum_{I,i\neq j,\sigma} J_{ij} \hat{c}^{\dagger}_{Ii\sigma} \hat{c}^{\dagger}_{Ij\bar{\sigma}} \hat{c}_{Ii\bar{\sigma}} \hat{c}_{Ij\sigma} + \\ &+ \frac{1}{2} \sum_{I,i,j,\sigma,\sigma'} V_{ij} \hat{n}_{Ii\sigma} \hat{n}_{\bar{I}j\sigma'} + \\ &+ \sum_{I,i\neq j,\sigma,\sigma'} J^{(exc)} \hat{c}^{\dagger}_{Ii\sigma} \hat{c}_{I\bar{i}\sigma} \hat{c}^{\dagger}_{\bar{I}j\sigma'} \hat{c}_{\bar{I}\bar{j}\sigma'}\end{aligned} \tag{1}$$

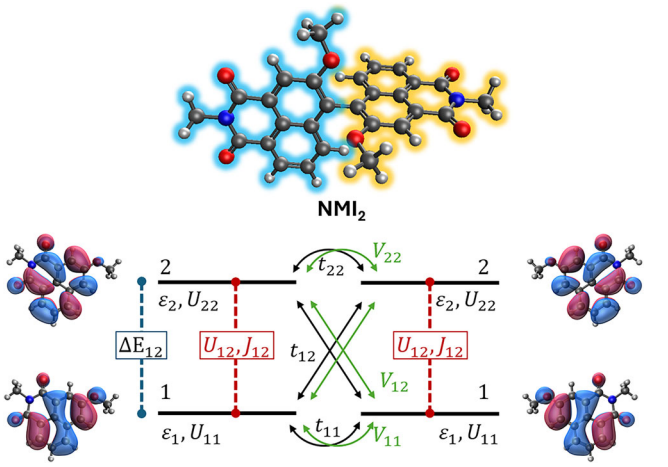


**Fig. 2 | The extended Hubbard model.** Schematic representation of the Hubbard-like model for $NMI_2$, described in Eq. (1), and HOMO and LUMO orbitals of NMI fragments, labeled 1 and 2, respectively.

where the upper case indices run on the two sites, lower case indices run on site orbitals, and $\sigma$ is the spin label, so that $\hat{c}^{\dagger}_{Ii\sigma}$, $\hat{c}_{Ii\sigma}$ and $\hat{n}_{Ii\sigma}$ are the creation, annihilation, and number operators for the $\sigma$-spin electron in the $i$-th spatial orbital of the $I$-th site. Barred indexes indicate the other possible value for the site, orbital or spin. The first line in Eq. (1) collects the one-electron terms of the Hamiltonian, where $\epsilon_i$ is the energy for the $i$-th site orbital (equal on both fragments), and $t_{ij}$ is the hopping integral between the $i$-th and $j$-th orbitals (on different fragments, on-site hopping integrals do vanish). The second and third lines of Eq. (1) collect the on-site two electron terms, with $U_{ij}$ measuring the repulsion between two electrons residing on the same site in the same or in different orbitals, and $J_{ij}$ is the on-site exchange coupling. The fourth line of Eq. (1) describes inter-site electrostatic interactions. The fifth line in Eq. (1) introduces exciton coupling, a two-electron term that describes the interaction between on-site transition dipole moments, parameterized by the exciton coupling energy $J^{(exc)}$. This term does not appear in the standard versions of the Hubbard model, but should be accounted for when several orbitals are present on each site. The derivation of this term and its relevance are discussed in the Section "Exciton coupling in Hubbard-like models" of the Supporting Information.

For the parametrization of the Hubbard Hamitonian, we rely on the complete active-space configuration interaction (CASCI) approach, widely adopted as a starting point for more refined computational techniques, such as RASCI and CASSCF. CASCI offers several advantages, such as size-insensitivity and comparatively well-behaved potential energy surfaces[36]. Moreover, it was successfully adopted to describe electronic excitations in dimers, a problem somehow relevant for our aim[37]. Specifically, we adopt CAS-sr-DFT, a variant of CASCI, to effectively account for dynamic correlation, by incorporating short range electron-electron interactions in a DFT framework[38]. The basis set for the CASCI and CAS-sr-DFT approaches are the electronic configurations, i.e., the states obtained populating the active orbitals with the proper number of electrons. The CASCI or CAS-sr-DFT eigenstates are obtained upon diagonalization of the relevant Hamiltonian matrix, that explicitly accounts for one- and two-electron terms. Specifically, in CAS-sr-DFT a range separation parameter is defined (we set it to 0.2 $a_0$ to best fit the experimental excitation energy of NMI) on the electron-electron distance, so that two-electron terms are calculated using DFT in the short range and wave function theory in the long range. Additional computational details can be found in Section "Additional results" of the Supporting Information, together with calculations for a larger active space including additional virtual orbitals (Table S10).

We adopt CAS(2,2)-sr-DFT calculations to describe each NMI fragment, i.e., including two orbitals, the HOMO and LUMO, and two electrons in the active space. Analogously, $NMI_2$ is described in CAS(4,4)-sr-DFT,

**Table 1 | Generalized Hubbard parameters**

| Generalized Hubbard parameters | | |
|---|---|---|
| $J_{12}$ | 0.22 | 0.22 |
| $U_{12}$ | 3.42 | 3.42 |
| $U_{11}$ | 3.54 | 3.54 |
| $U_{22}$ | 3.41 | 3.41 |
| $\Delta E_{12}$ | 3.40 | 3.40 |
| $t_{11}$ | −0.16 | −0.16 |
| $t_{12}$ | −0.14 | −0.14 |
| $t_{22}$ | −0.03 | −0.08 |
| $V_{11}$ | 2.06 | 2.06 |
| $V_{22}$ | 2.21 | 2.22 |
| $V_{12}$ | 2.09 | 2.10 |
| $J^{(exc)}$ | 0.03 | - |
| RMSE | 0.05 | 0.05 |
| RMSE' | 0.02 | 0.04 |

Hubbard parameters (eV) extracted as described in Section "Model Hamiltonian". Parameters in the first column are obtained using the full Hamiltonian in Eq. (1), parameters in the second column are obtained neglecting exciton coupling. The last two lines show the root mean squared error calculated accounting for all transition energies (RMSE) and for the four lowest excited states (RMSE').

accounting for 4 orbitals, HOMO-1, HOMO, LUMO and LUMO+1, and 4 electrons. As a first step, we run an HF calculation (6-31G(d) basis set) on the isolated NMI fragment and on a NMI ⋯ NMI system, corresponding to two NMI fragments set to a large distance ( ~ 20 Å). This procedure allowed us to verify that the pair-degenerate canonical orbitals of NMI ⋯ NMI do coincide with the canonical orbitals of the isolated NMI, so that all intersite interactions can be safely neglected in the NMI ⋯ NMI pair. The energy of the configurations $E_i$ (the basis state of the CAS-CI calculation) can be obtained rotating the eigenvalues of a CAS(4,4)-sr-DFT calculation on NMI ⋯ NMI on the configuration basis, as follows:

$$E_i = \sum_a |c_{ia}|^2 \epsilon_a \tag{2}$$

where $i$ and $a$ run on the configurations and eigenstates, respectively, $c_{ia}$ is an element of the eigenvector matrix, and $\epsilon_a$ is the $a$-th CAS-CI eigenvalue. Once the energies of the configurations are known, the on-site parameters ($U_{ij}$, $t_{ij}$, $J_{ij}$ in Eq. (1)) can be easily obtained, as described in Section "Extraction of on-site parameters" in the Supporting Information.

Inter-site model parameters ($t_{ij}$, $V_{ij}$, $J^{(exc)}$) rely on CAS(4,4)-sr-DFT calculation on $NMI_2$ and are extracted adjusting the inter-site model parameters of the Hamiltonian in Eq. (1) as to best fit the ab initio transition energies, while maintaining the on-site parameters fixed to the values obtained from NMI ⋯ NMI results. Results are listed in Table 1. A good agreement is obtained in terms of the energy (RMSE of ~0.045 eV) and of the nature of the states, estimated in terms of the weight of charge resonance states on the CAS(4,4)-sr-DFT states compared to the Hubbard states (Table S7).

Results in Table 1 show that the inclusion of the exciton coupling term in our Hamiltonian marginally affects the global quality of the fit, while it definitely improves the the description of the lowest-lying excited states (i.e., the pair of local triplet states and the pair of local singlet states), suggesting that the exciton coupling is required for a reliable description of the low energy excited states. Moreover, accounting for exciton coupling does not significantly affect inter-site parameters with the only exception of $t_{22}$, that goes from ~80 meV if the exciton coupling is disregarded, to ~30 meV if it is accounted for.

Overall, Hubbard eigenstates are a good approximation of CAS-sr-DFT eigenstates. Minor deviations can be ascribed to two main sources: (1) the MOs of $NMI_2$ that enter the active space in the CAS(4,4)-sr-DFT calculation are not exactly linear combination of the same on-site orbitals that enter the CAS(2,2)-sr-DFT calculation on the NMI dimer, and (2) some of the two electron integrals that enter the CASCI calculations are not included in the *neglect differential overlap* approximation adopted in the Hubbard model[22,23].

Eq. (1) allows to tackle the many-body nature of the states of homodimers, as needed, e.g., to address spectroscopy, however SOC interactions must be properly accounted for to describe CISS. The general expression for the one-electron SOC Hamiltonian reads:

$$\mathcal{H}_{SO} = \sum_{i\sigma,j\sigma'} \langle i\sigma|\hat{h}_{SO}|j\sigma'\rangle \hat{c}^{\dagger}_{i\sigma}\hat{c}_{j\sigma'} \tag{3}$$

Where $i$ and $j$ indexes run on site orbitals, while $\sigma$ and $\sigma'$ run on spin. Therefore the definition of the SOC operator amounts to the determination of the one-electron integrals $\langle i\sigma|\hat{h}_{SO}|j\sigma'\rangle$. Towards this aim, we perform a DFT calculation on $NMI_2$ (B3LYP/6-31G(d), ORCA package[39,40]) to extract the one-electron SOC operator written on the basis of DFT orbitals. By visual inspection (Fig. S7) and relying on symmetry considerations, the $NMI_2$ frontier MO can be approximated as linear combinations of the NMI orbitals as follows:

$$\begin{cases} |\,\text{HOMO-1}\,\rangle & \approx \frac{1}{\sqrt{2}}\left(|\text{homo}_a\rangle + |\text{homo}_b\rangle\right) \\ |\,\text{HOMO}\,\rangle & \approx \frac{1}{\sqrt{2}}\left(|\text{homo}_a\rangle - |\text{homo}_b\rangle\right) \\ |\,\text{LUMO}\,\rangle & \approx \frac{1}{\sqrt{2}}\left(|\text{lumo}_a\rangle + |\text{lumo}_b\rangle\right) \\ |\,\text{LUMO+1}\,\rangle & \approx \frac{1}{\sqrt{2}}\left(|\text{lumo}_a\rangle - |\text{lumo}_b\rangle\right) \end{cases} \tag{4}$$

where upper and lower case letters refer to the MO of $NMI_2$ and NMI, respectively, and $a$ and $b$ refer to the two NMI sites. A straightforward basis rotation then allows to obtain the desired SOC matrix elements (SOCMEs) on the basis of the NMI site orbitals. Not surprisingly, the estimated SOC values are fairly small (Fig. S5). The largest contribution to SOC is due to its component aligned along the charge transfer axis (the long axis in our reference frame). Specifically, the $\langle \text{lumo}_a|\hat{h}_{SO,z}|\text{lumo}_b\rangle$ integral is 1.1 $cm^{-1}$, with a SOC-to-hopping ratio ~0.005, a small number that is however surprisingly large for organic molecules. As expected, the information on chirality of the system is encoded in the sign of SOC, as shown in Fig. S6, where two out of the three cartesian components of SOC change in sign upon changing the enantiomer.

### The role of SOC and correlation

SOC interactions, although typically weak in $\pi$-conjugated organic systems, are essential to achieve spin polarization. Often, when modeling chiral systems as Hubbard chains with one orbital per site with nearest-neighbor (NN) hopping, a next-nearest-neighbor (NNN) SOC is included[13,15,19]. Historically, this approach stems from the influential model by Kane and Mele for spin polarization in graphene[41]. From a symmetry standpoint, purely NN SOC and hopping terms lead to spin-independent Hamiltonians, so that the introduction of a NNN term (hopping, SOC, or both) is required to achieve non-negligible spin polarization. When multiple orbitals per site are considered, like in the model presented in Section "Model Hamiltonian", the connectivity of the hopping and SOC operators effectively leads to different channels for SOC and hopping.

While the form of hopping and SOC operators in principle may lead to non-negligible spin-polarization for the $NMI_2$ bridge modeled as in Section "Model Hamiltonian", this does not guarantee that high spin polarizations can be achieved. Indeed, theoretical approaches based on single-electron models consistently failed to quantitatively reproduce experiments where high spin polarization is measured. We therefore investigate the role of correlations in our study. Diagonalizing the model

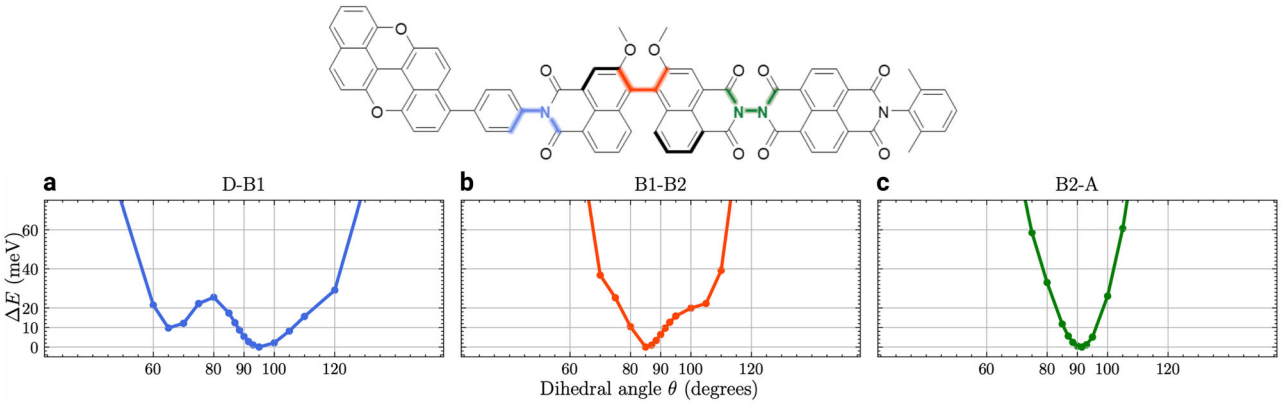


**Fig. 3 | Rigid energy scans for torsions around the PXX-NMI, NMI-NMI, and NMI-NDI bonds.** Top: The Kekulè structure of PNN with the bonds involved in the three conformational degrees of freedom are highlighted with different colors. Bottom: Rigid potential energy scans as a function of the three dihedral angles connecting the subunits of PNN: a) Donor-Bridge, b) intra-Bridge, and c) Bridge-Acceptor.

in eq. (1) with parameters in Table 1 for a system of four electrons produces a singlet ground state, where each of the two lowest-energy orbitals, localized on separate sites, is occupied by two electrons. This state is separated by a large energy gap of ~3.1 eV from the first excited triplet (Table S7). In order to simulate PET, we should consider an additional electron coming from the photoexcited donor. This electron will travel through the empty orbitals of the bridge, since the energy gap to involve the occupied orbital is too large (comparable to $\Delta\varepsilon_{21}$ as shown in Section "Assessing the role of electron-electron correlations" of the Supporting Information). Accordingly, a significant role of electron correlations in PET dynamics can be excluded, despite the large values for the two-electron terms ($U_{ij}$, $J_{ij}$, and $V_{ij}$) found for $NMI_2$. While electron correlations are not relevant in the $NMI_2$ bridge, $J$ and $U$ play an important role in amplifying spin polarization in systems where orbitals are degenerate or separated by small gaps[15].

### The role of molecular vibrations: assessing low frequency modes

Having excluded a significant role of electron correlation in PET, we therefore turn our attention to another possible source of amplified spin polarization, namely low-energy vibrational modes interacting with electrons[13,14]. The important role of vibrations in the CISS effect is also suggested by the increase of spin polarization with temperature observed in some experiments[42].

The DFT analysis of vibrational modes of PNN in its ground-state geometry shows that low energy modes primarily involve the torsional motions around the bonds between molecular fragments. Specifically, the torsion around the donor-bridge bond mainly contributes to a mode with harmonic frequency 1.2 meV, the torsion between the two NMI fragments contributes to a mode at 1.76 meV and the torsion around the bridge-acceptor bond contributes to a mode at 3.72 meV, as displayed in Fig. S8. These torsional modes are particularly relevant to PET dynamics since they modulate the conjugation between the weakly coupled units of the system, as depicted in Fig. 3. To better investigate their nature beyond the harmonic approximation, we computed variation of the energy of the system as a function of the dihedral angle, describing the relative rotation between these units. This was done through a rigid scan, where all other atomic coordinates were kept fixed at their equilibrium values. Figure 3 collects the resulting rigid energy scans for the selected three conformational modes (the same scans on a wider range are shown in Fig. S9). Torsions around the bridge-acceptor bond lead to symmetric and harmonic potential energy scans (Fig. 3c), indicating elastic behavior and fairly rigid bonds. This is probably due to strong steric repulsion between the oxygen atoms of the carbonyl groups. Conversely, the torsion between the NMI units inside the bridge, shows a marked anharmonicity and asymmetry (Fig. 3b), with the system favoring twisting towards higher angles (i.e., methoxy-groups further apart). This asymmetry clearly results from axial chirality of the $NMI_2$ unit. Finally, torsions around the donor-bridge bond lead a flat, anharmonic curve characterized by a double minimum (Fig. 3a and Fig. S9), indicative of significant thermal conformational disorder, suggesting that, even at low temperatures, the molecule can explore a large configurational space. This asymmetry is only apparent: the donor-bridge bond shows no axial chirality. If all possible conformers were taken into account, symmetric behavior would be recovered.

### Electron-vibration coupling

Electron-vibration coupling is addressed in parametric Hamiltonians, like the generalized Hubbard model in Section "Model Hamiltonian", selecting few relevant vibrational modes and accounting for the variation of models parameters when moving along the corresponding coordinate. In the context of site-models, like the Hubbard model or few state models for electron transfer, often one distinguishes between Holstein modes, that modulate the site energy, and Peierls modes, that modulate off-diagonal matrix elements (including the hopping integrals and the SOCMEs), while, typically, the modulation of two electron terms is neglected. For PNN, in close analogy with what observed in chemically related TADF dyes[43,44], the twists around the bond connecting two $\pi$-conjugated moieties are identified as key Peierls modes. Specifically, in the $NMI_2$ unit, we identify the relevant Peierls mode as the torsion around the bond connecting the two NMI units. The assessment of electron correlations presented above indicates that electron transfer through the $NMI_2$ bridge occurs via a single channel, with electrons hopping between the LUMOs of the NMI units. For this reason, here we obtain a preliminary estimate on the dependence of the LUMO-LUMO hopping ($t_{LL}$) and SOC ($h_{SO}^{(LL)}$) on twists around the NMI-NMI bond (Fig. 4). A well-established approach to estimate the hopping integral between degenerate site orbitals relies on the same approximation as in Eq. (4), considering that LUMO and LUMO + 1 of $NMI_2$ are symmetric and antisymmetric combinations of the LUMOs on the NMI sites. In this approximation, $t_{LL}$ is estimated as half the splitting between LUMO and LUMO + 1 of $NMI_2$. The reduced SOCME between LUMOs of neighboring NMI units is obtained as

$$h_{RSO}^{(LL)} = \sqrt{|h_{SO,x}^{(LL)}|^2 + |h_{SO,y}^{(LL)}|^2 + |h_{SO,z}^{(LL)}|^2} \quad (5)$$

where $h_{SO,\alpha}^{(LL)}$ is the $\alpha$ cartesian component of the SOCME between LUMOs of neighboring NMI units.

Results in Fig. 4 show that $t_{LL}$ strongly depends on the torsional mode, being almost linear in close proximity to the equilibrium geometry (~100°, marked in Fig. 4 with a vertical dashed line. (The equilibrium value of the dihedral is different than the one marked in Fig. 3 for the PNN complex, as

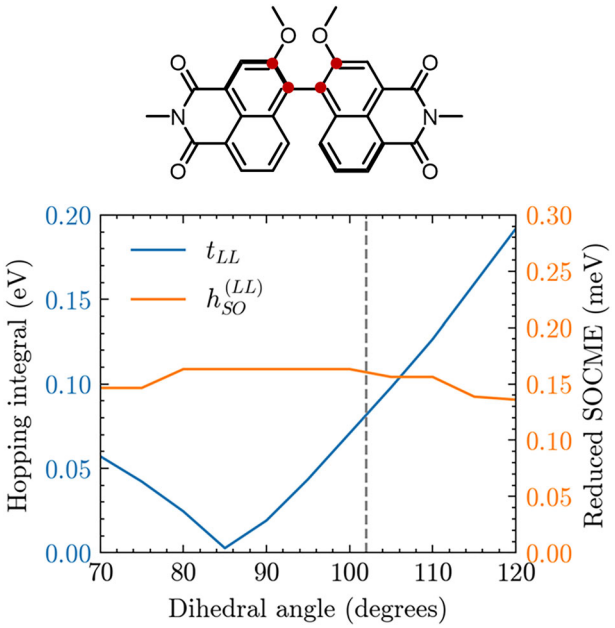


**Fig. 4 | Hopping and spin-orbit coupling as a function of the NMI-NMI torsion.** Hopping integral (blue, left *y*-axis) and reduced SOCME (orange, right *y*-axis) between on-site LUMO orbitals in the $NMI_2$ dimer as a function of the dihedral angle between NMI fragments. The atoms used to define the dihedral are highlighted in red in the Kekulè structure. The dashed gray line marks the value of the dihedral at the ground state equilibrium geometry.

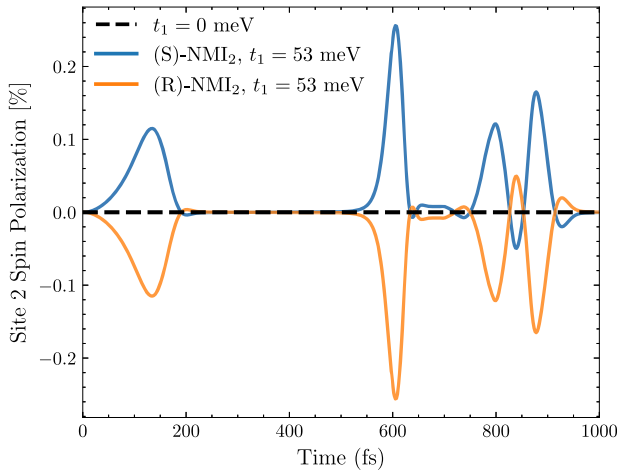


**Fig. 5 | Spin polarization over time in the $NMI_2$ bridge.** Spin polarization at site 2 of the bridge obtained from unitary time evolution over 1000 fs. The black line represents the dynamics without electron-vibration coupling, while the blue and orange lines include it with a hopping term of $t_1 = 53$ meV for the (S) and (R) enantiomers, respectively.

here the scan is performed on the isolated $NMI_2$). Conversely, $h_{SO}^{(LL)}$ is constant over all the explored range of the torsional motion. Due to the different dependence of hopping (real) and SOC (imaginary), the phase of the total complex diabatic coupling is modulated by twists around the NMI-NMI bond. Quite interestingly, a similar modulation of the phase of the diabatic coupling was identified to lead to spin polarization in electron transport in single-channel one-electron models near conical intersections[45]. While this is a promising result, it does not directly apply to the present study. Here, we explore the effects of modulation by a Peierls mode of the diabatic phase from a different perspective. Building on the conclusions of Section "The role of SOC and correlation", we find that, upon excitation of the PXX unit, an electron is injected into the $NMI_2$ bridge. This reduces the problem to a single electron moving between the two LUMO levels of $NMI_2$. To describe this process, we consider an effective model that explicitly incorporates a torsional vibrational mode between the $NMI_2$ units. The Hamiltonian governing this system is given by:

$$\begin{aligned}\mathcal{H} = &\sum_{\substack{I=1,2\\ \sigma}} \varepsilon_I \hat{c}_{I\sigma}^\dagger \hat{c}_{I\sigma} - t_0 \sum_\sigma \left(\hat{c}_{1\sigma}^\dagger \hat{c}_{2\sigma} + \hat{c}_{2\sigma}^\dagger \hat{c}_{1\sigma}\right) + \\ &- t_1 \sum_\sigma \left(\hat{c}_{1\sigma}^\dagger \hat{c}_{2\sigma} + \hat{c}_{2\sigma}^\dagger \hat{c}_{1\sigma}\right) \frac{1}{\sqrt{2}} \left(\hat{a}^\dagger + \hat{a}\right) + \\ &+ \hbar\omega \left(\hat{a}^\dagger \hat{a} + \frac{1}{2}\right) + \frac{k_4}{4} \left(\hat{a}^\dagger + \hat{a}\right)^4 + \\ &- i\lambda_z \left(\hat{c}_{1\uparrow}^\dagger \hat{c}_{2\uparrow} - \hat{c}_{1\downarrow}^\dagger \hat{c}_{2\downarrow}\right) + \\ &- i\lambda_x \left(\hat{c}_{1\uparrow}^\dagger \hat{c}_{2\downarrow} + \hat{c}_{1\downarrow}^\dagger \hat{c}_{2\uparrow}\right) + \text{h.c.}\end{aligned} \tag{6}$$

where $I$ runs on the two sites of the bridge and $\sigma$ denotes the spin label. The first two terms, previously introduced in Eq. (1), now specifically describe the two LUMO levels of the bridge. The third term accounts for the electron-vibration interaction, which is modeled as a linear coupling between the electronic hopping and the nuclear coordinate $\hat{Q} = \frac{1}{\sqrt{2}}\left(\hat{a}^\dagger + \hat{a}\right)$, with $\hat{a}^\dagger$ and $\hat{a}$ being the bosonic creation and annihilation operators, respectively. The coupling strength is determined by the parameter $t_1$. The fourth and fifth terms define the vibrational Hamiltonian, respectively corresponding to the harmonic oscillator Hamiltonian with frequency $\omega$ and to a quartic correction. The final two terms incorporate the SOC along $z$ (the charge transfer direction) and $x$ axes, respectively. The $y$ component of the SOC is not present, as it is predicted to be zero for $NMI_2$ from ab initio calculations (Fig. S5 and Fig. S6). The details about the ab initio parametrization of this Hamiltonian can be found in Section "Parametrizing electron-vibration coupling" of the Supporting Information. The ab initio extracted parameters (summarized in Table S8) are $\hbar\omega = 1.52$ meV, $t_0 = -79$ meV, $t_1 = -53$ meV, $\lambda_z = 0.136$ meV, $\lambda_x = 0.082$ meV, $\varepsilon_1 = \varepsilon_2$. The quartic term $k_4$ serves solely as a numerical tool to confine the harmonic potential and is set to 0.1 meV.

To verify whether electron-vibration coupling alone can induce a finite in spin polarization we simulate the unitary evolution of the system starting from the initial density operator

$$\hat{\rho}(0) = \left\{\frac{1}{2}|1,\uparrow\rangle\langle 1,\uparrow| + \frac{1}{2}|1,\downarrow\rangle\langle 1,\downarrow|\right\}_{\text{el}} \otimes \{|0\rangle\langle 0|\}_{\text{vib}}. \tag{7}$$

This is a product electro-nuclear state with electrons occupying the up and down spin orbitals on site 1 with equal probability, and the void vibrational state. This *unpolarized out-of-equilibrium* state naturally arises from the photoexcitation of an electron into the donor LUMO, followed by an incoherent transfer to the first site of the bridge via a spin-independent jump operator of the form $\hat{X}_D = \sum_\sigma \hat{c}_{1\sigma}^\dagger \hat{c}_{D\sigma} + h.c.$ To track the spin dynamics, we define the spin polarization operator on a site $I$ as $\hat{P}_I = \hat{c}_{I\uparrow}^\dagger \hat{c}_{I\uparrow} - \hat{c}_{I\downarrow}^\dagger \hat{c}_{I\downarrow}$. In Fig. 5, we present the time evolution of $\langle \hat{P}_I \rangle_t = Tr[\hat{\rho}(t)\hat{P}_I]$ turning off (i) and on (ii) the electron-vibration coupling $t_1 = 53$ meV, as extracted from ab initio calculations (Section "Parametrizing electron-vibration coupling" of the Supporting Information). In the latter case, we consider both enantiomers by changing the sign of the SOC in the Hamiltonian.

The simulations highlight the crucial role of electron-vibration coupling in the emergence of spin polarization within the CISS framework in PET. As expected, for $t_1 = 0$ (case i) the spin polarization is zero, because the Hamiltonian reduces to a single-channel model in which the SOC can be traced out via a gauge transformation, eventually leading to a spin-independent Hamiltonian[10,46–48]. On the other hand, (case ii) when a Peierls mode is explicitly included, finite oscillations of the spin polarization are obtained. Moreover, changing the enantiomer reverses the sign of the spin polarization, as expected.

These findings provide key qualitative insights. Typically, models for CISS rely on a multi-channel configuration (NNN interactions or multiple orbitals per site) to break the single-channel no-go theorem and obtain spin polarization. Conversely, here we show that an analogous effect can be realized by explicitly incorporating vibronic levels and electron-vibration coupling. Indeed, in this case each site hosts multiple electro-vibrational states, as illustrated in Fig. S11. In this framework, Peierls coupling introduces non-trivial connectivity and multi-channel behavior, thus establishing oscillations in the spin polarization within the chiral bridge. This is a necessary condition for spin polarization to accumulate on the acceptor once additional incoherent relaxation pathways are introduced.

In summary, our preliminary analysis of electron-vibration coupling in the $NMI_2$ chiral bridge reveals that low-frequency modes strongly coupled to the electronic degrees of freedom can play an important role in the CISS mechanism in small molecules, laying the ground for future studies on the role of electron-vibration coupling in CISS.

## Conclusions

In this work, we consider a specific system, PNN, where CISS was observed upon PET. For this system, we introduce a generalized Hubbard model to describe the chiral bridge involved in the electron transfer process, i.e., the $NMI_2$ fragment. Reliable model parameters are obtained through an original procedure (Section 4.3 of the Supporting Information), that exploits complete active space methods, where dynamic correlations are effectively taken into account treating short range electron-electron interaction with DFT. The derivation of the on-site parameters is exact, while intersite parameters are obtained via an eigenvalue fitting procedure, yielding a good agreement between the Hubbard model and CAS-CI eigenstates. This approach could be extended to other homo- and etero-dimers or larger molecular aggregates. The Hubbard model in Eq. (1), along with its generalization in Eq. S1, provides a powerful framework for addressing important problems in materials science, energy conversion, and quantum information. For instance, it can be applied to study symmetry-breaking charge transfer in null aggregates[16] and singlet fission[49,50]. In such cases, understanding the interactions between localized, excitonic, and charge resonance states with different spin multiplicities is crucial for determining the photophysics of the system. As for CISS, SOC is predicted to be small in the $NMI_2$ bridge, as expected for $\pi$-conjugated systems. However, strong correlations are found, with $U$ values that range in the order of 3.4 eV. Despite this, the large HOMO-LUMO gap of NMI leads to a single channel for electron transfer, and thus leads to very small spin polarizations. Due to the limited effect of correlations in the $NMI_2$ bridge, the role of molecular vibrations is addressed. As expected for large molecules composed of almost orthogonal $\pi$-conjugated moieties, many low frequency modes can affect the Hubbard parameters. In particular, torsions around the bonds that connect $\pi$-conjugated molecules are relevant, as they can show strong anharmonicity and flat potential energy regions, as well as tune the conjugation between neighboring $\pi$-conjugated molecules, thus significantly impacting diabatic and spin-orbit interactions that contribute to electron transfer. The simple model presented in Section "The role of molecular vibrations: assessing low frequency modes" shows how this kind of molecular vibration can lead to non-negligible spin polarization even in one-electron systems with NN hopping and SOC, possibly suggesting a mechanism for CISS in small organic molecules characterized by axial chirality. These findings open new avenues for exploring the role of low-frequency vibrations in the mechanism establishing spin polarization.

## Methods

Geometry optimizations, TD-DFT, torsional potential energy scans, and CASCI calculations were performed with the Q-Chem software package (version 6.1)[51]. Optimized geometries are provided in Section 8 of the Supplementary Information. SOC calculations in Sections "Model Hamiltonian" and "Electron-vibration coupling" were performed using the ORCA package (version 5.0.2)[40]. The DFT calculations presented in Section 3 of the Supporting Information, calculation of normal modes reported in Section "The role of molecular vibrations: assessing low frequency modes", and torsional potential energy scans were conducted at the B3LYP/6-31G(d) level. The normal mode presented in Sections "Electron-vibration coupling" and 6 of the Supporting Information is obtained with the Gaussian package (version 16 Revision B.01)[52] at the def2tzvp-B3LYP level.

### Supporting information

The authors have cited additional references within the Supporting Information[38,52–66].

## Data availability

The data that support the findings of this study are available at the following link https://doi.org/10.5281/zenodo.15268096.

Received: 8 November 2024; Accepted: 30 April 2025;
Published online: 28 May 2025

## References

1. Ray, K., Ananthavel, S. P., Waldeck, D. H. & Naaman, R. Asymmetric scattering of polarized electrons by organized organic films of chiral molecules. *Science* **283**, 814–816 (1999).
2. Yang, S.-H., Naaman, R., Paltiel, Y. & Parkin, S. S. P. Chiral spintronics. *Nat. Rev. Phys.* **3**, 328–343 (2021).
3. Chiesa, A. et al. Chirality-induced spin selectivity: an enabling technology for quantum applications. *Adv. Mater.* **35**, e2300472 (2023).
4. Naaman, R., Paltiel, Y. & Waldeck, D. H. Chiral induced spin selectivity and its implications for biological functions. *Annu. Rev. Biophys.* **51**, 99–114 (2022).
5. Pacchioni, G. Chirality-induced spin selectivity enables real-time monitoring of a chemical reaction. *Nat. Rev. Mater.* **8**, 364–364 (2023).
6. Bloom, B. P., Chen, Z., Lu, H. & Waldeck, D. H. A chemical perspective on the chiral induced spin selectivity effect. *Natl Sci. Rev.* **11**, nwae212 (2024).
7. Eckvahl, H. J. et al. Direct observation of chirality-induced spin selectivity in electron donor-acceptor molecules. *Science* **382**, 197–201 (2023).
8. Eckvahl, H. J., Copley, G., Young, R. M., Krzyaniak, M. D. & Wasielewski, M. R. Detecting chirality-induced spin selectivity in randomly oriented radical pairs photogenerated by hole transfer. *J. Am. Chem. Soc.* **146**, 24125–24132 (2024).
9. Gutierrez, R., Díaz, E., Naaman, R. & Cuniberti, G. Spin-selective transport through helical molecular systems. *Phys. Rev. B* **85**, 081404 (2012).
10. Guo, A.-M. & Sun, Q.-f Spin-selective transport of electrons in DNA double helix. *Phys. Rev. Lett.* **108**, 218102 (2012).
11. Geyer, M., Gutierrez, R. & Cuniberti, G. Effective Hamiltonian model for helically constrained quantum systems within adiabatic perturbation theory: Application to the chirality-induced spin selectivity (CISS) effect. *J. Chem. Phys.* **152**, 214105 (2020).
12. Fransson, J. Chirality-induced spin selectivity: the role of electron correlations. *J. Phys. Chem. Lett.* **10**, 7126–7132 (2019).
13. Fransson, J. Vibrational origin of exchange splitting and "chiral-induced spin selectivity". *Phys. Rev. B* **102**, 235416 (2020).
14. Zhang, L., Hao, Y., Qin, W., Xie, S. & Qu, F. Chiral-induced spin selectivity: a polaron transport model. *Phys. Rev. B* **102**, 214303 (2020).
15. Chiesa, A. et al. Many-body models for chirality-induced spin selectivity in electron transfer. *Nano Lett.* **24**, 12133–12129 (2024).
16. Spano, F. C. Symmetry-breaking charge separation and null aggregates. *J. Phys. Chem. C.* **128**, 248–260 (2024).
17. Smith, M. B. & Michl, J. Singlet fission. *Chem. Rev.* **110**, 6891–6936 (2010).
18. Sun, H., Zhong, C. & Bredas, J.-L. Reliable prediction with tuned range-separated functionals of the singlet–triplet gap in organic

emitters for thermally activated delayed fluorescence. *J. Chem. Theory Comput.* **11**, 3851–3858 (2015).
19. Fransson, J. Charge redistribution and spin polarization driven by correlation induced electron exchange in chiral molecules. *Nano Lett.* **21**, 3026–3032 (2021).
20. Alwan, S., Sharoni, A. & Dubi, Y. Role of electrode polarization in the electron transport chirality-induced spin-selectivity effect. *J. Phys. Chem. C.* **128**, 6438–6445 (2024).
21. Hubbard, J. Electron correlations in narrow energy bands. *Proc. R. Soc. Lond. Ser. A Math. Phys. Sci.* **276**, 238–257 (1963).
22. Kivelson, S., Su, W.-P., Schrieffer, J. R. & Heeger, A. J. Missing bond-charge repulsion in the extended Hubbard model: effects in polyacetylene. *Phys. Rev. Lett.* **58**, 1899–1902 (1987).
23. Painelli, A. & Girlando, A. Interacting electrons in 1d: applicability of hubbard models. *Synth. Met.* **27**, A15–A20 (1988).
24. Pariser, R. & Parr, R. G. A semi-empirical theory of the electronic spectra and electronic structure of complex unsaturated molecules. I. *J. Chem. Phys.* **21**, 466–471 (1953).
25. Pople, J. A. Electron interaction in unsaturated hydrocarbons. *Trans. Faraday Soc.* **49**, 1375–1385 (1953).
26. Soos, Z. G. & Klein, D. J. Modified Hubbard model for complex TCNQ salts. *J. Chem. Phys.* **55**, 3284–3290 (1971).
27. Fortunelli, A. & Painelli, A. Ab initio estimate of Hubbard model parameters: mA simple procedure applied to BEDT-TTF salts. *Phys. Rev. B* **55**, 16088–16095 (1997).
28. Soos, Z. G., Hayden, G. W., Girlando, A. & Painelli, A. Pariser–parr–pople force field for $\pi$-electrons: Raman and infrared shifts of trans-polyacetylene. *J. Chem. Phys.* **100**, 7144–7152 (1994).
29. Barford, W. & Chambers, C. A. Theory of singlet fission in carotenoid dimers. *J. Chem. Phys.* **159**, 084116 (2023).
30. Bedogni, M., Giavazzi, D., Di Maiolo, F. & Painelli, A. Shining light on inverted singlet–triplet emitters. *J. Chem. Theory Comput.* **20**, 902–913 (2023).
31. Dubbini, M., Bonvini, F., Savi, L. & Di Maiolo, F. Turning on organic radical emitters. *J. Phys. Chem. C* **128**, 18158–18169 (2024).
32. Green, J. D. & Hele, T. J. Exroppp: Fast, accurate, and spin-pure calculation of the electronically excited states of organic hydrocarbon radicals. *J. Chem. Phys.* **160**, 164110 (2024).
33. Chiesa, A., Carretta, S., Santini, P., Amoretti, G. & Pavarini, E. Many-body models for molecular nanomagnets. *Phys. Rev. Lett.* **110**, 157204 (2013).
34. Chiesa, A., Carretta, S., Santini, P., Amoretti, G. & Pavarini, E. Many-body ab initio study of antiferromagnetic $Cr_7M$ molecular rings. *Phys. Rev. B* **94**, 224422 (2016).
35. Garlatti, E. et al. Anisotropy of coii transferred to the cr7co polymetallic cluster via strong exchange interactions. *Chem. Sci.* **9**, 3555–3562 (2018).
36. Levine, B. G., Durden, A. S., Esch, M. P., Liang, F. & Shu, Y. CAS without scf—why to use CASCI and where to get the orbitals. *J. Chem. Phys.* **154**, 090902 (2021).
37. Parker, S. M., Seideman, T., Ratner, M. A. & Shiozaki, T. Communication: active-space decomposition for molecular dimers. *J. Chem. Phys.* **139**, 021108 (2013).
38. Casanova, D. Short-range density functional correlation within the restricted active space CI method. *J. Chem. Phys.* **148**, 124118 (2018).
39. De Souza, B., Farias, G., Neese, F. & Izsak, R. Predicting phosphorescence rates of light organic molecules using time-dependent density functional theory and the path integral approach to dynamics. *J. Chem. Theory Comput.* **15**, 1896–1904 (2019).
40. Neese, F., Wennmohs, F., Becker, U. & Riplinger, C. The ORCA quantum chemistry program package. *J. Chem. Phys.* **152**, 224108 (2020).
41. Kane, C. L. & Mele, E. J. Quantum spin hall effect in graphene. *Phys. Rev. Lett.* **95**, 226801 (2005).
42. Das, T. K., Tassinari, F., Naaman, R. & Fransson, J. Temperature-dependent chiral-induced spin selectivity effect: experiments and theory. *J. Phys. Chem. C.* **126**, 3257–3264 (2022).
43. Dhali, R. et al. Understanding TADF: a joint experimental and theoretical study of DMAC-TRZ. *Phys. Chem. Chem. Phys.* **23**, 378–387 (2021).
44. Phan Huu, D. K. A., Saseendran, S. & Painelli, A. Effective models for TADF: the role of the medium polarizability. *J. Mater. Chem. C.* **10**, 4620–4628 (2022).
45. Wu, Y. & Subotnik, J. E. Electronic spin separation induced by nuclear motion near conical intersections. *Nat. Commun.* **12**, 700 (2021).
46. Meyer, J. S., Falko, V. I. & Altshuler, B. L. Quantum in-plane magnetoresistance in 2d electron systems. In *Strongly Correlated Fermions and Bosons in Low-Dimensional Disordered Systems*, Vol. 72 of *NATO Science Series II* (eds Lerner, I. V., Altshuler, B. L., Falko, V. I. & Giamarchi, T.) 117–164 (Springer, 2002).
47. Gutierrez, R. et al. Modeling spin transport in helical fields: derivation of an effective low-dimensional Hamiltonian. *J. Phys. Chem. C.* **117**, 22276–22284 (2013).
48. Matityahu, S., Utsumi, Y., Aharony, A., Entin-Wohlman, O. & Balseiro, C. A. Spin-dependent transport through a chiral molecule in the presence of spin-orbit interaction and nonunitary effects. *Phys. Rev. B* **93**, 075407 (2016).
49. Casanova, D. Theoretical modeling of singlet fission. *Chem. Rev.* **118**, 7164–7207 (2018).
50. Dill, R. D., Smyser, K. E., Rugg, B. K., Damrauer, N. H. & Eaves, J. D. Entangled spin-polarized excitons from singlet fission in a rigid dimer. *Nat. Commun.* **14**, 1180 (2023).
51. Epifanovsky, E. et al. Software for the frontiers of quantum chemistry: an overview of developments in the Q-Chem 5 package. *J. Chem. Phys.* **155**, 084801 (2021).
52. Frisch, M. J. et al. Gaussian¯16 Revision B.01 (2016). Gaussian Inc. Wallingford CT.
53. Valentini, C. et al. Customising excitation properties of polycyclic aromatic hydrocarbons by rational positional heteroatom doping: the peri-xanthenoxanthene (PXX) case. *Chem. Sci.* **13**, 6335–6347 (2022).
54. Plasser, F. Theodore: a toolbox for a detailed and automated analysis of electronic excited state computations. *J. Chem. Phys.* **152**, 084108 (2020).
55. Dev, P., Agrawal, S. & English, N. J. Determining the appropriate exchange-correlation functional for time-dependent density functional theory studies of charge-transfer excitations in organic dyes. *J. Chem. Phys.* **136**, 224301 (2012).
56. Tozer, D. J. Relationship between long-range charge-transfer excitation energy error and integer discontinuity in Kohn-Sham theory. *J. Chem. Phys.* **119**, 12697–12699 (2003).
57. Dreuw, A. & Head-Gordon, M. Single-reference ab initio methods for the calculation of excited states of large molecules. *Chem. Rev.* **105**, 4009–4037 (2005).
58. Phan Huu, D. A. et al. Antiadiabatic view of fast environmental effects on optical spectra. *Phys. Rev. Lett.* **124**, 107401 (2020).
59. Tirado-Rives, J. & Jorgensen, W. L. Performance of b3lyp density functional methods for a large set of organic molecules. *J. Chem. Theory Comput.* **4**, 297–306 (2008).
60. Hussein, H. A. A DFT study of structural stability, Mulliken charges, MEP, FMO, and NLO properties of trans alkenyl substituted chalcones conformers: theoretical study. *Struct. Chem.* **34**, 2201–2223 (2023).
61. Davydov, A. S. The theory of molecular excitons. *Sov. Phys. Uspekhi* **7**, 145 (1964).
62. Kasha, M., Rawls, H. R. & Ashraf El-Bayoumi, M. The exciton model in molecular spectroscopy. *Pure Appl. Chem. VIIIth* **11**, 371–392 (1965).
63. Spano, F. C. The spectral signatures of Frenkel polarons in H-and J-aggregates. *Acc. Chem. Res.* **43**, 429–439 (2010).

64. Bertocchi, F., Sissa, C. & Painelli, A. Circular dichroism of molecular aggregates: a tutorial. *Chirality* **35**, 681–691 (2023).
65. Vosko, S. H., Wilk, L. & Nusair, M. Accurate spin-dependent electron liquid correlation energies for local spin density calculations: a critical analysis. *Can. J. Phys.* **58**, 1200–1211 (1980).
66. Grimme, S., Antony, J., Ehrlich, S. & Krieg, H. A consistent and accurate ab initio parametrization of density functional dispersion correction (DFT-D) for the 94 elements H-Pu. *J. Chem. Phys.* **132**, 154104 (2010).

## Acknowledgements

D.K.A.P.H., A.Ca., P.B., A.Ch., A.P., and S.C. acknowledge funding by the Horizon Europe Programme within the ERC-Synergy project CASTLE (proj. n. 101071533). Views and opinions expressed are however those of the author(s) only and do not necessarily reflect those of the European Union or the European Commission. Neither the European Union nor the granting authority can be held responsible for them. D.K.A.P.H., L.S., and A.P. also acknowledge funding from PNRR MUR project PE0000023-NQSTI and from the equipment and framework of the COMP-HUB and COMP-R Initiatives, funded by the "Departments of Excellence program of the Italian Ministry for University and Research" (MIUR, 2018–2022 and MUR, 2023–2027). A.Ch. also acknowledges funding from the University of Parma through the action Bando di Ateneo 2024 per la ricerca. This research benefits from the High Performance Computing facility of the University of Parma, Italy.

## Author contributions

A.Ch. and S.C. developed the core concepts and research questions. D.K.A.P.H. and A.Ch. designed the model in Eq. (1). A.Ca. and P.B. performed DFT and TD-DFT calculations. D.K.A.P.H. developed the computational framework for the parametrization of the model, with support by A.Ca. and L.S. in the CAS calculations. P.B., A.Ch., A.P., and S.C. supervised the project providing ongoing guidance and support. S.C. and A.P. secured the funding for this project. D.K.A.P.H. and A.Ca. wrote the initial draft of the manuscript and designed the figures. All authors contributed to review and editing.

## Competing interests

The authors declare no competing interests.

## Additional information

**Supplementary information** The online version contains supplementary material available at https://doi.org/10.1038/s43246-025-00821-3.

**Correspondence** and requests for materials should be addressed to Stefano Carretta.

**Peer review information** *Communications Materials* thanks Longlong Zhang, Hua-Hua Fu and the other, anonymous, reviewer(s) for their contribution to the peer review of this work. Primary Handling Editor: Aldo Isidori. A peer review file is available.